

Chapter 2

Spectroscopic-Imaging STM (SI-STM)

In this chapter I detail the main experimental technique used in this thesis: Spectroscopic-Imaging Scanning Tunnelling Microscopy (SI-STM). I outline the theoretical basis for its use as a tunnelling spectroscopy of superconductors as well as data analysis techniques specific to cuprate superconductors. I also give details of the cuprate samples studied.

Scanning tunnelling microscopy (STM) is a technique which uses the tunnelling current of electrons between a sharp metal tip and a sample to image its surface [1]. An exponential dependence of the tunnelling current on the distance between tip and sample makes the STM very sensitive to small changes in surface topography, allowing atomic resolution imaging. STM can also act as a spectroscopic tool by using the tunnel junction between tip and sample to carry out tunnelling conductance spectroscopy, revealing information about the electronic states contributing to the tunnelling current. The advantage of performing spectroscopy with an STM is that it can be done with atomic resolution. The theoretical basis for the topographic and spectroscopic capabilities of STM are outlined in this chapter.

STM came to take a prominent role in the study of quantum matter with the advent of spectroscopic imaging STM (SI-STM) [2, 3]. In SI-STM the topographic and spectroscopic abilities of the STM are systematically combined. The sample's surface topography and spectroscopic information are obtained simultaneously across a two-dimensional grid of points, or pixels. In doing so, one is essentially visualising the energy-resolved density of states of electrons in the material. In this chapter I will detail the techniques needed to obtain both real and momentum space information about the wave-functions in cuprate superconductors.

The rapid and fairly specialised development of the field means that for completeness I must touch on a fairly large number of sub-topics, some of which are fairly technical; one way to use this chapter might be to back-reference to it from the main results chapters of the thesis rather than try to take in every detail on first reading.

2.1 Quantum Tunnelling as a Spectroscopy

The experiments presented in this thesis rely on measuring the tunnelling current of electrons between a sample and a metal electrode across an insulating barrier [4, 5]. The tunnelling process consists of transferring an electron from a many-body state that is localised in the left electrode to another many-body state localised in the right electrode. Of course, by symmetry we expect the reverse process to have an equal rate, resulting in zero net current. However, under external application of a bias such as a current or voltage this symmetry is broken resulting in a net a current.

The variation of the current with the applied bias can yield information about the many-body states involved. Calculating the rates of these tunnelling processes from first principles is not generally possible. In the following section I will describe the tunnelling Hamiltonian formalism that can be used to extract spectroscopic information from the tunnelling current, without exactly solving the tunnelling problem [6, 7].

2.1.1 Tunnelling Hamiltonian Formalism

Within the tunnelling Hamiltonian formalism, the total Hamiltonian is given by

$$\hat{H} = \hat{H}_L + \hat{H}_R + \hat{H}_T, \quad (2.1)$$

where \hat{H}_L and \hat{H}_R describe the many-body states in the left and right electrodes separately, in the absence of each other [7]. \hat{H}_T contains all additional terms that arise from coupling the electrodes to each other through the tunnel junction.

An exact treatment of this problem for two interacting many-body states in the right and left electrodes is not generally analytically tractable. Instead, we can treat \hat{H}_T perturbatively. Typically we use a tunnelling Hamiltonian of the form,

$$\hat{H}_T = \sum_{i,j} \left(M_{i,j} \hat{c}_{L,i}^\dagger \hat{c}_{R,j} + M_{j,i}^* \hat{c}_{R,j}^\dagger \hat{c}_{L,i} \right), \quad (2.2)$$

where $\hat{c}_{L,i}^\dagger$ creates an electron in state i on the left electrode and $\hat{c}_{R,j}^\dagger$ creates an electron in state j on the right electrode [7]. I will now examine the consequences of this Hamiltonian for various choices of the Hamiltonians \hat{H}_L and \hat{H}_R corresponding to Normal-Insulator-Normal (NIN), Superconductor-Insulator-Normal (SIN) and Superconductor-Insulator-Superconductor (SIS) tunnel junctions.

2.1.2 Normal-Insulator-Normal (NIN) Tunnelling

In the case of two normal metal electrodes the Hamiltonians are given by

$$\hat{H}_L = \sum_{\vec{k}} \epsilon_{\vec{k}} \hat{c}_{L,\vec{k}}^\dagger \hat{c}_{L,\vec{k}} \quad (2.3)$$

$$\hat{H}_R = \sum_{\vec{q}} \epsilon_{\vec{q}} \hat{c}_{R,\vec{q}}^\dagger \hat{c}_{R,\vec{q}} \quad (2.4)$$

$$\hat{H}_T = \sum_{\vec{k},\vec{q}} \left(M_{\vec{k},\vec{q}} \hat{c}_{L,\vec{k}}^\dagger \hat{c}_{R,\vec{q}} + M_{\vec{q},\vec{k}}^* \hat{c}_{R,\vec{q}}^\dagger \hat{c}_{L,\vec{k}} \right) \quad (2.5)$$

where $\hat{c}_{L,\vec{k}}^\dagger$ creates an electron of crystal momentum \vec{k} in the left electrode with energy ϵ_k measured relative to the Fermi energy. Here, spin indices have been suppressed under the assumption that no spin-flip processes take place in tunnelling.

We can then perturbatively calculate the current of electrons from the left to the right electrode using Fermi's golden rule as

$$I_{L \rightarrow R} = \frac{2\pi e}{\hbar} \sum_{\vec{k},\vec{q}} |M_{\vec{k},\vec{q}}|^2 f_{\vec{k}} [1 - f_{\vec{q}}] \delta(\epsilon_{\vec{k}} - \epsilon_{\vec{q}}), \quad (2.6)$$

where $f_{\vec{k}}$ is the occupation number of the state \vec{k} . Similarly, the reverse current is given by

$$I_{R \rightarrow L} = \frac{2\pi e}{\hbar} \sum_{\vec{k},\vec{q}} |M_{\vec{k},\vec{q}}|^2 f_{\vec{q}} [1 - f_{\vec{k}}] \delta(\epsilon_{\vec{q}} - \epsilon_{\vec{k}}), \quad (2.7)$$

with the net current from left to right given by $I = I_{L \rightarrow R} - I_{R \rightarrow L}$.

Under the simplifying assumption that $T = 0$ and the matrix elements, $|M_{\vec{k},\vec{q}}| = |M|$, are a constant for states within eV of the chemical potential then this reduces to the form

$$I = \frac{2\pi e}{\hbar} |M|^2 \int_0^{eV} n_L(\epsilon + eV) n_R(\epsilon) d\epsilon, \quad (2.8)$$

where $n(\epsilon)$ is the momentum integrated density of states at energy ϵ [7].

Under a further assumption that we choose a right hand electrode with a constant density of states $n_R(E) = n_R(0)$, then Eq. 2.8 becomes

$$I = \frac{2\pi e}{\hbar} |M|^2 n_R(0) \int_0^{eV} n_L(\epsilon + eV) d\epsilon \quad (2.9)$$

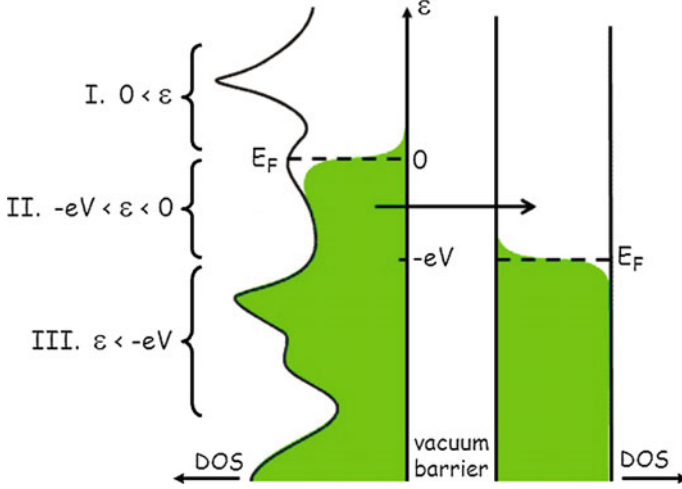


Fig. 2.1 Schematic of tunnelling from *left hand* electrode with negative bias applied, to *right hand* electrode. *Green shading* indicates filled states. Only energy ranges where left-hand states are filled and right-hand states are empty (i.e. region II) contribute to the net tunnelling current. The *right hand* density of states (DOS) is drawn flat as is required if useful spectroscopic information is to be obtained without deconvolution. Figure adapted from Ref. [8]

and $n_L(E)$ can be measured directly through the differential tunnelling conductance

$$\frac{dI}{dV} = \frac{2\pi e^2}{\hbar} |M|^2 n_R(0) n_L(eV). \quad (2.10)$$

The physical tunnelling processes resulting in these equations are depicted in Fig. 2.1. Tunnelling may only occur from filled states to empty states. Hence by applying a positive bias we are probing the empty states of the left electrode (or sample) and with a negative bias its filled states.

The assumption of an energy independent matrix element, $|M_{\vec{k},\vec{q}}| = |M|$, is not in any sense innocuous. For metals described by the independent-particle pictures used in Eqs. 2.3 and 2.4, Harrison calculated the matrix elements $M_{\vec{k},\vec{q}}$ within the WKB approximation [9]. The conclusion was that the energy dependence of the matrix elements exactly cancels that of the density of states. This results in featureless, ohmic tunnelling $I(V)$ curves.

On the face of it, this would indicate that we cannot use tunnelling as a spectroscopy on metals. However, if the sample we wish to measure is not a single-band metal, well described by a Fermi liquid, then the cancellation between the density of states and the matrix element does not hold and spectroscopy becomes possible [6, 7, 9]. Specifically, Eqs. 2.9 and 2.10 which we derived for metals of independent electrons, are actually also valid for tunnelling between a superconductor and a normal metal electrode. In the next section I will outline why this is the case.

2.1.3 Superconductor-Insulator-Normal (SIN) Tunnelling

Now I will discuss tunnelling between a normal metal and a superconductor. This is the configuration of electrodes used in the STM studies of cuprate superconductors in Chap. 4, where a tungsten tip is used to perform spectroscopy on cuprate superconductor samples. In this case the normal and superconducting electrode Hamiltonians, \hat{H}_N and \hat{H}_S , are given by

$$\hat{H}_N = \sum_{\vec{q}} \epsilon_{\vec{q}} \hat{c}_{L,\vec{q}}^\dagger \hat{c}_{L,\vec{q}} \quad (2.11)$$

$$\hat{H}_S = \sum_{\vec{k}} E_{\vec{k}} (\hat{\alpha}_{\vec{k}}^\dagger \hat{\alpha}_{\vec{k}} + \hat{\beta}_{\vec{k}}^\dagger \hat{\beta}_{\vec{k}}) \quad (2.12)$$

where

$$\alpha_{\vec{k}} = u_{\vec{k}} \hat{c}_{R,\vec{k},\uparrow} - v_{\vec{k}} \hat{c}_{R,-\vec{k},\downarrow}^\dagger \quad (2.13)$$

$$\beta_{\vec{k}} = u_{\vec{k}} \hat{c}_{R,-\vec{k},\downarrow} + v_{\vec{k}} \hat{c}_{R,\vec{k},\uparrow}^\dagger \quad (2.14)$$

and $u_{\vec{k}}$ and $v_{\vec{k}}$ are the BCS coherence factors [7, 10].

As presented in Chap. 1, the ground state of condensed pairs in the superconducting electrode is described by the BCS wave-function [10]. Its Bogoliubov quasiparticle excitations are a superposition of holes and electrons and are annihilated by the $\alpha_{\vec{q}}$ and $\beta_{\vec{q}}$ operators. Their energy spectrum is given by

$$E_{\vec{k}} = \sqrt{\epsilon_{\vec{k}}^2 + |\Delta|^2} \quad (2.15)$$

where $\epsilon_{\vec{k}}$ are the single-particle energies of the normal state band from which the superconducting instability arises and Δ is the superconducting gap.

In order to consider the current between the electrodes arising from the tunnelling Hamiltonian it is convenient to define new operators which definitely create either an electron or hole in the superconductor, rather than a superposition of the two [11, 12]. These four operators are

$$\hat{\alpha}_{e,\vec{k}}^\dagger = u_{\vec{k}}^* \hat{c}_{\vec{k}\uparrow}^\dagger - v_{\vec{k}}^* \hat{S}^\dagger \hat{c}_{-\vec{k}\downarrow} \quad (2.16)$$

$$\hat{\alpha}_{h,\vec{k}}^\dagger = u_{\vec{k}}^* \hat{S} \hat{c}_{\vec{k}\uparrow}^\dagger - v_{\vec{k}}^* \hat{c}_{-\vec{k}\downarrow} \quad (2.17)$$

$$\hat{\beta}_{e,\vec{k}}^\dagger = u_{\vec{k}}^* \hat{c}_{-\vec{k}\downarrow}^\dagger + v_{\vec{k}}^* \hat{S}^\dagger \hat{c}_{\vec{k}\uparrow} \quad (2.18)$$

$$\hat{\beta}_{h,\vec{k}}^\dagger = u_{\vec{k}}^* \hat{S} \hat{c}_{-\vec{k}\downarrow}^\dagger + v_{\vec{k}}^* \hat{c}_{\vec{k}\uparrow} \quad (2.19)$$

where $\hat{\alpha}_{e,\vec{k}}^\dagger$ creates an electron with wave-vector \vec{k} and \hat{S}^\dagger adds a Cooper-pair to the condensate. We can invert these definitions to express the electron creation operator in terms of the new operators, yielding

$$\hat{c}_{k\uparrow}^\dagger = u_{\vec{k}} \hat{\alpha}_{e,\vec{k}}^\dagger + v_{\vec{k}}^* \hat{\beta}_{h,\vec{k}}. \quad (2.20)$$

Now consider a term in the tunnelling Hamiltonian $M_{\vec{k},\vec{q}} \hat{c}_{L,q}^\dagger \hat{c}_{R,k}$. Using Eq. 2.20 this will contribute a term in the current proportional to $|u_{\vec{k}}|^2 |M_{\vec{k},\vec{q}}|^2$ because the second term in Eq. 2.20 annihilates the BCS ground state. The physical interpretation of the coefficient $|u_{\vec{k}}|^2$ is that it is the probability that a state \vec{k} is not occupied in the BCS wave-function and hence is able to accept an incoming electron.

The coherence factors $u_{\vec{k}}$ and $v_{\vec{k}}$, which encode details of the superconducting wave-function, actually drop out of the full expression for the tunnelling current to leave a remarkably simple result. There is another state \vec{k}' with $E_{\vec{k}'} = E_{\vec{k}}$ but with $\epsilon_{\vec{k}'} = -\epsilon_{\vec{k}}$. This will contribute to the current a term $|u_{\vec{k}'}|^2 |M_{\vec{k}',\vec{q}}|^2 = |v_{\vec{k}}|^2 |M_{\vec{k},\vec{q}}|^2$ because $|u(-\epsilon)| = |v(\epsilon)|$. If $|M_{\vec{k}',\vec{q}}| \approx |M_{\vec{k},\vec{q}}|$, since \vec{k} and \vec{k}' are near the same point on the Fermi surface then the total contribution from these two terms will be proportional to $(|u_{\vec{k}}|^2 + |v_{\vec{k}}|^2) |M_{\vec{k},\vec{q}}|^2 = |M_{\vec{k},\vec{q}}|^2$ because $|u_{\vec{k}}|^2 + |v_{\vec{k}}|^2 = 1$ as a result of fermionic particle statistics.

At $T = 0$ this independence of the coherence factors results in an SIN current

$$I_{SIN} = \frac{2\pi e}{\hbar} \sum_{\vec{k},\vec{q}} |M_{\vec{k},\vec{q}}|^2 \delta(E_{\vec{k}} - |\epsilon_{\vec{q}}|). \quad (2.21)$$

From this it is evident that we can treat the tunnelling from a normal metal into a superconductor as if the superconductor were described by independent particles in a semiconductor with density of states

$$\frac{n_s(E)}{n_{s0}} = \begin{cases} \frac{E}{\sqrt{E^2 - |\Delta|^2}} & E > |\Delta| \\ 0 & E < |\Delta| \end{cases} \quad (2.22)$$

Here $n_s(E)$ is the Bogoliubon density of states and n_{s0} the density of states of the underlying normal band, assumed to be constant. Here I show the result for an s -wave superconducting gap. For a d -wave gap $n_s(E)$ can simply be replaced by the d -wave Bogoliubon density of states.

Under the assumption that $|M_{\vec{k},\vec{q}}| = |M|$, we arrive at

$$I_{SIN} = \frac{2\pi e}{\hbar} |M|^2 \int_0^{eV} n_s(\epsilon + eV) n_n(\epsilon) d\epsilon, \quad (2.23)$$

which is the same form for the tunnelling current derived for a metal of non-interacting quasi-particles derived in Sect. 2.1.2. If we choose a normal metal

electrode with a constant density of states n_0 (such as a tungsten STM tip) then the differential tunnelling conductance

$$\frac{dI}{dV} = \frac{2\pi e^2}{\hbar} |M|^2 n_0 n_s(eV) \quad (2.24)$$

measures $n_s(E)$ directly [6, 7, 9, 12].

2.1.4 Superconductor-Insulator-Superconductor (SIS) Tunnelling

If we only consider the tunnelling of single electrons between two superconducting electrodes then the semiconductor model presented in the previous section still holds due to a similar simplification of the coherence factors [13]. This results in a superconductor-insulator-superconductor tunnelling current

$$I_{SIS} = \frac{2\pi e}{\hbar} |M|^2 \int_0^{eV} n_{S1}(E - eV) n_{S2}(E) dE. \quad (2.25)$$

$n_{S1}(E)$ and $n_{S2}(E)$ would be given by Eq. 2.22 with superconducting gaps Δ_1 and Δ_2 respectively. Neither of the electrodes has a constant density of states near the Fermi energy, resulting in a more complicated expression for the differential tunnelling current [13]:

$$\frac{dI}{dV} = \frac{2\pi e^2}{\hbar} |M|^2 \left[n_{S1}(E) n_{S2}(E + eV) + \int_0^{eV} n_{S1}(E) \frac{d}{d(eV)} n_{S2}(E + eV) dE \right]. \quad (2.26)$$

This will be used in Chap. 5 for the scanned Josephson tunnelling microscope, which uses a superconducting STM tip to measure a superconducting sample.

In addition to the single electron tunnelling processes between superconductors considered here, there is also the possibility of the tunnelling of Cooper-pairs between the electrodes [11]. This is known as the Josephson effect and it will be discussed in Chap. 5, where I will demonstrate the use of Cooper-pair tunnelling to directly visualise the Cooper-pair condensate in $\text{Bi}_2\text{Sr}_2\text{CaCu}_2\text{O}_{8+\delta}$.

Having outlined the theoretical basis for vacuum tunnelling and its use as a spectroscopy I will now go on to describe how it is used in an STM.

2.2 STM - Principles

The STM consists of a sharp conducting tip that can be rastered across a conducting sample surface. This is typically achieved by attaching the tip to a piezoelectric

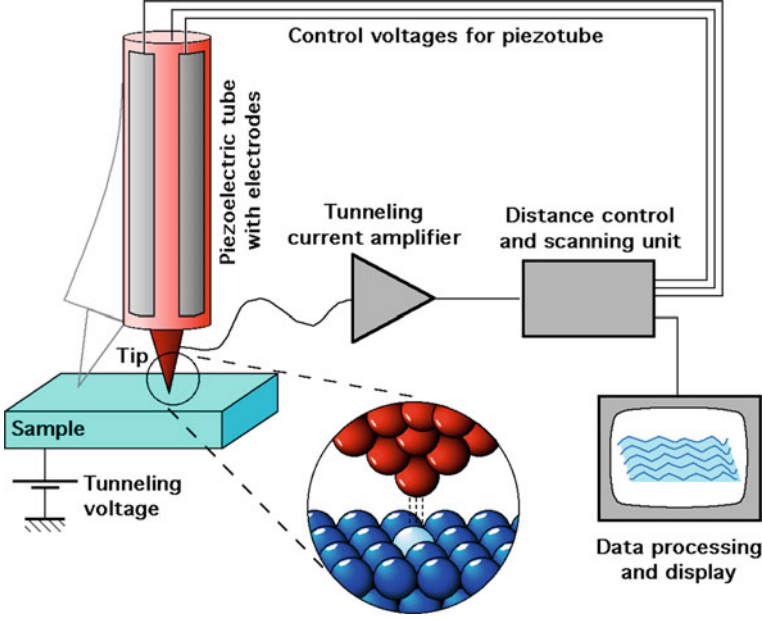


Fig. 2.2 Schematic of STM operation. This figure illustrates tunnelling between a voltage-biased sample and an atomically sharp tip. In constant current operation the piezoelectric tube is used to scan the tip in the x and y directions. As this is done the tunnelling current is measured. A feedback system (PID) is used to adjust z using the piezo-tube so as to keep the current constant. Reproduced from Ref. [14]

scanner tube as shown schematically in Fig. 2.2 [1]. A bias voltage, V , is applied between the two and the vacuum tunnelling current measured. We shall see below that its utility as an extremely sensitive topographic probe derives from the exponential dependence of the tunnelling current on the tip-sample distance. The principles of tunnelling spectroscopy detailed in the previous section can also be applied to STM to give access to the atomically resolved local density of states (LDOS).

Focussing on the case of SIN tunnelling between a normal metal STM tip and a superconducting sample pertinent to Chap. 4, the elastic tunnelling current between tip and sample under applied bias voltage V at $T = 0$ is

$$I_{SIN}(\vec{r}, z, E = eV) = \frac{2\pi e}{\hbar} n_T(0) |M(\vec{r}, z)|^2 \int_0^{eV} n_S(\vec{r}, \epsilon) d\epsilon. \quad (2.27)$$

$n_s(\vec{r}, E)$ is the superconducting LDOS of the sample at position $\vec{r} = (x, y)$, z is the tip-sample separation and energy $E = eV$. The density of states of the STM tip, n_T , has been taken to be constant here. In the measurements presented in this thesis this was achieved using tungsten STM tips which have a flat density of states

near the Fermi energy. Thus, we see that at a given position, $I_{SIN}(\vec{r}, z, V)$ is directly proportional to the energy-integrated density of states.

The spatially resolved differential tunnelling conductance is given by

$$g(\vec{r}, z, E = eV) = \frac{2\pi e^2}{\hbar} |M(\vec{r}, z)|^2 n_0 n_S(\vec{r}, E = eV). \quad (2.28)$$

Thus at a given position, $g(\vec{r}, V)$ is directly proportional to the local density of states $n_S(\vec{r}, E)$.

To see why STM is such an effective atomic scale probe we now need to examine the dependence of the matrix elements $|M(\vec{r}, z)|$ on the tip sample distance z . Bardeen has shown [6] that if the many-body tip and sample states are known then in principle the matrix elements $|M_{\mu\nu}|$ can be calculated via

$$M_{\mu\nu} = \frac{\hbar^2}{2m} \int d\vec{S} \cdot (\psi_\mu^* \nabla \psi_{\nu u} - \psi_\nu \nabla \psi_{\mu u}^*), \quad (2.29)$$

where the integral is over any surface lying entirely within the vacuum region. These wave-functions are typically not known but an analytical model that provides much insight was provided by Tersoff and Hamann [15]. They showed that

$$|M_{\mu\nu}|^2 \propto \exp(-2\kappa z), \quad (2.30)$$

where $\kappa = \sqrt{\frac{2m\phi}{\hbar^2}}$ with ϕ being the work functions of the tip and sample (which are assumed to be the same), z the tip-sample distance and m the electron mass. κ^{-1} represents the maximum decay length of sample wave-functions into the vacuum.

This exponential decay with z is what we might have expected from considering a simple 1D square barrier of height ϕ within the WKB approximation. It gives STM an extreme sensitivity to changes in the topographic height of the sample. Below I will discuss how Eqs. 2.27, 2.28 and 2.30 are utilised in the topographic and spectroscopic imaging modalities of STM.

2.3 STM - Modes of Operation

2.3.1 Topography

To record a topograph a set-point bias V_s is applied between tip and sample. A feedback loop is then used to keep $I(\vec{r}, Z, eV_s)$ constant at a set-point value I_s , by varying z , as the tip rasters across a sample [16]. In this way one is able to resolve sub-Angström changes in sample topography. An STM topograph, $T(\vec{r})$, consists of an image in which each pixel at position \vec{r} records the value of z required to attain the set-point current.

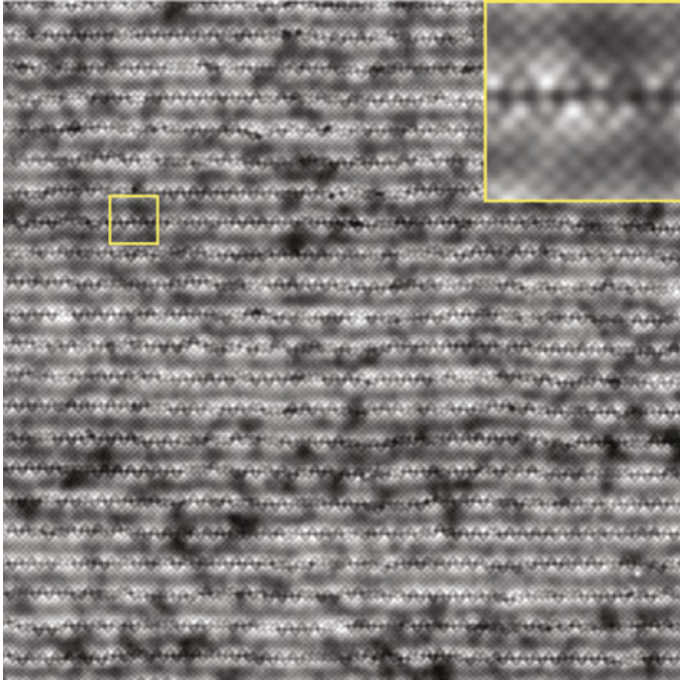


Fig. 2.3 Atomically resolved topograph, $T(\vec{r})$, of a $\text{Bi}_2\text{Sr}_2\text{CaCu}_2\text{O}_{8+\delta}$ sample in a $65 \times 65 \text{ nm}$ field of view. *Inset* is magnified image of the section outlined in yellow

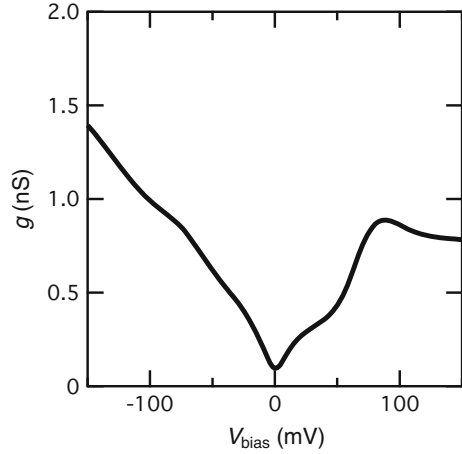
Let us term $\int_0^{eV_s} n_S(\epsilon, \vec{r}) d\epsilon$ the integrated LDOS. If this and the matrix element are uniform across the sample then the STM “topograph” will be a good approximation to the true topography of the surface.

Figure 2.3 shows an atomically resolved topograph of the BiO surface of $\text{Bi}_2\text{Sr}_2\text{CaCu}_2\text{O}_{8+\delta}$. Here the atomic contrast is known to result from the Bi atoms on the insulating surface layer. This layer does not contribute to the low energy LDOS and hence the atomic contrast in Fig. 2.3 must arise through atomic scale variations in the tunnelling matrix elements.

2.3.2 Spectroscopy

As shown above in Eq. 2.28, the differential conductance $g(\vec{r}, V) = dI(\vec{r}, z, V)/dV$ at bias voltage V is proportional to $n_S(\vec{r}, eV)$. Thus by holding the tip at constant z , sweeping the bias voltage and recording $g(\vec{r}, V)$ one can measure $n_S(\vec{r}, eV)$ [16]. While it is possible to measure $I(\vec{r}, z, V)$ and then take a numerical derivative to give $g(\vec{r}, V)$, a considerably better signal to noise ratio can be obtained by using a small AC modulation of V from a lock-in amplifier to measure this quantity directly. Let $V(t) = V_0 + V_m \cos(\omega t + \phi)$ then,

Fig. 2.4 Typical differential conductance spectrum, $g(V)$, for a $\text{Bi}_2\text{Sr}_2\text{CaCu}_2\text{O}_{8+\delta}$ sample with $p = 6\%$



$$I(\vec{r}, z, V(t)) = I(\vec{r}, z, V_0) + \left. \frac{dI(\vec{r}, z, V)}{dV} \right|_{V_0} V_m \cos(\omega t + \phi) + \left. \frac{d^2 I(\vec{r}, z, V)}{dV^2} \right|_{V_0} \frac{V_m^2}{2} \cos^2(\omega t + \phi) + \dots, \quad (2.31)$$

and hence measurement of the amplitude of the first harmonic gives $g(\vec{r}, z, V)$.

Taking a measurement of this type at a single point on the sample, \vec{r} , for a range of DC bias voltages results in a conductance spectrum, proportional to the LDOS, such as that shown in Fig. 2.4. I will now go on to discuss the systematic collection of these conductance spectra on a fine array of points on the sample to allow an energy resolved visualisation of the electronic structure. This is known as spectroscopic imaging STM (SI-STM).

2.4 SI-STM

In spectroscopic imaging STM (SI-STM) current and conductance spectra, $I(\vec{r}, z, E = eV)$ and $g(\vec{r}, z, E = eV)$, are collected on a fine 2D array of points on the sample to provide energy resolved maps of the local density of states and its integral [2, 3]. Simultaneously, a topographic image is also collected so that the spectroscopic maps can be registered to the lattice.

The procedure for collecting data of this type is as follows:

1. Define an regular array of points $\vec{r}_1, \vec{r}_2 \dots \vec{r}_N$ on the surface of the sample where measurements will be made. Each of these points will form a pixel in the resulting spectroscopic maps and simultaneous topograph.
2. Specify a set-point voltage and current, V_s and I_s , which will be used at all pixels to establish a tunnel junction. With the feedback loop turned on and a bias voltage V_s applied, the tip is moved to the first point in the measurement array and allowed to attain the set-point current I_s by varying z .

3. The feedback loop is then turned off and the value of z recorded as $T(\vec{r}_1)$.
4. An AC voltage modulation is then added to the DC bias. The DC bias V_0 is sequentially moved through a series of values $V_1, V_2, \dots, V_i, \dots, V_M$, pausing at each to average and record the values of current and differential conductance as $I(\vec{r}_1, E_i = eV_i)$ and $g(\vec{r}_1, E_i = eV_i)$. These are the spectra that make up the first pixel of the spectroscopic maps $I(\vec{r}, E)$ and $g(\vec{r}, E)$.
5. Ramp voltage back to V_S , turn on feedback loop and move to next pixel in array. Repeat steps 3–5 until a measurement has been made at every pixel.

The results of this procedure are spectroscopic maps $I(\vec{r}, E)$ and $g(\vec{r}, E)$ measured for $\vec{r} = \vec{r}_1, \vec{r}_2, \dots, \vec{r}_N$ and $E = eV_1, V_2, \dots, V_i, \dots, V_M$, as well as the simultaneous topograph $T(\vec{r})$. The SI-STM data collection modality and resultant data are depicted in Fig. 2.5.

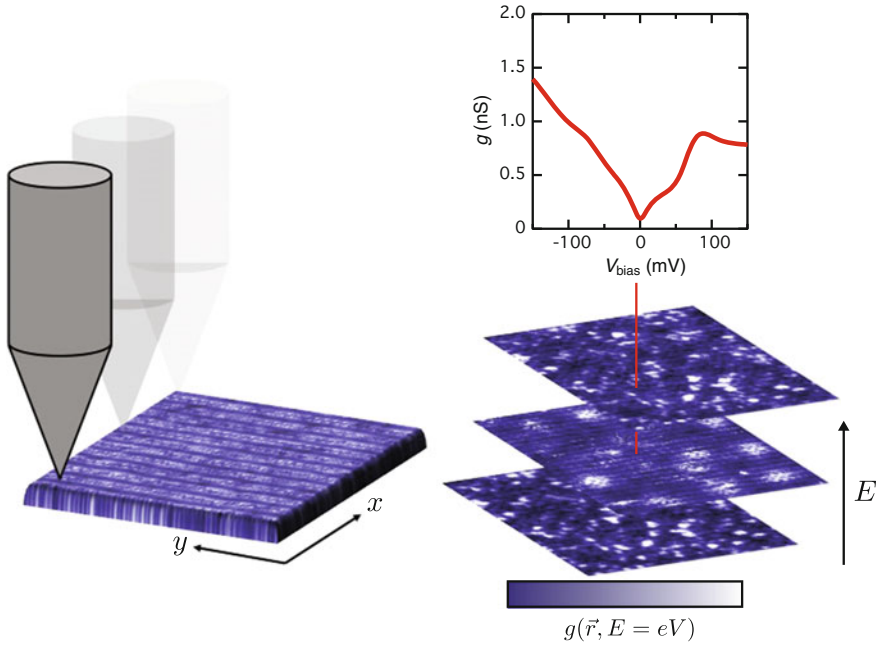


Fig. 2.5 Schematic illustration of SI-STM. The STM tip sequentially establishes a junction at an array of points on the surface of the sample and records current and conductance spectrum at each. This results in spectroscopic maps $I(\vec{r}, E)$ and $g(\vec{r}, E)$ as well as a simultaneous topograph $T(\vec{r})$. $g(\vec{r}, E)$ is shown on the *left hand side* in three dimensions (x, y, E). The *colour* scale in each slice corresponds to $g(\vec{r}, E)$ at a fixed energy. The *red line* parallel to the energy axis shows the path through this 3D space which results in the conductance spectrum (also shown in *red*) at a fixed point on the sample

2.4.1 The Setup Effect

SI-STM provides energy resolved electronic structure images that can be used to identify the presence of LDOS modulations. However the protocol described above, by which a tunnelling junction is established in SI-STM, can imprint conductance modulations from one set of energies onto another. This systematic error, which results in a misidentification of the energy of states undergoing spatial modulations, is called the setup effect. Therefore, determining the physically real modulations and especially their correct energies can present a grave challenge. Ignoring the setup effect, as is often the case, leads to incorrect characterisation of the electronic structure of materials.

The basic observable in STM experiments is the tunnelling current, $I(\vec{r}, z, E = eV)$, which depends on the bias between the tip and the sample, V , the tip sample separation, z , and the position on the sample surface, $r = (x, y)$, according to

$$I(\vec{r}, z, V) = f(\vec{r}, z) \int_0^{eV} n(\vec{r}, \epsilon) d\epsilon. \quad (2.32)$$

The function $f(\vec{r}, z)$ captures spatial variations due to surface corrugation, work function, matrix elements and proximity z of the tip to the surface. The integral of the LDOS, $\int_0^{eV} n(\vec{r}, \epsilon) d\epsilon$, includes spatial variation of the electronic structure.

SI-STM entails establishing a stable tunnel junction at every \vec{r} by using the same set-point current and bias voltage I_S and V_S . These set-point values then constrain the pre-factor of the integral in Eq. 2.32 via

$$I(\vec{r}, z, V_S) = I_S = f(\vec{r}, z) \int_0^{eV_S} n(\vec{r}, \epsilon) d\epsilon \quad (2.33)$$

$$\Rightarrow f(\vec{r}, z) = \frac{I_S}{\int_0^{eV_S} n(\vec{r}, \epsilon) d\epsilon} \quad (2.34)$$

and thus the expressions for $I(\vec{r}, E = eV)$ and $g(\vec{r}, E = eV)$ are given by

$$I(\vec{r}, E = eV) = I_S \frac{\int_0^{eV} n(\vec{r}, \epsilon) d\epsilon}{\int_0^{eV_S} n(\vec{r}, \epsilon) d\epsilon} \quad (2.35)$$

$$g(\vec{r}, E = eV) = I_S \frac{n(\vec{r}, eV)}{\int_0^{eV_S} n(\vec{r}, \epsilon) d\epsilon}. \quad (2.36)$$

The term in the denominator is responsible for the setup effect since it imprints the integral of the LDOS over the range of energies 0 to eV_S onto every energy in $I(\vec{r}, E = eV)$ or $g(\vec{r}, E = eV)$.

Figure 2.6 demonstrates how the choice of setup bias to establish the tunnelling junction strongly influences the acquired data. While both the left and right panels are spatial images of $g(\vec{r}, E = eV)$ taken at $V = 50$ mV in the same field of view,

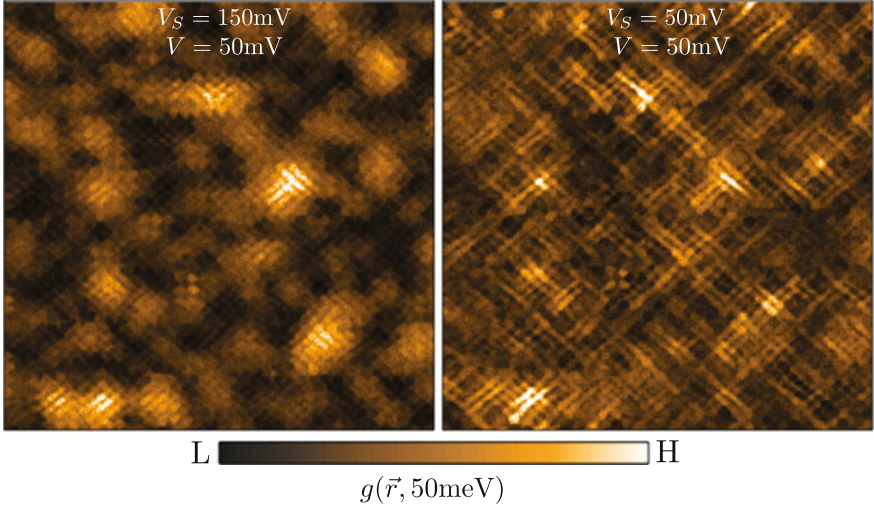


Fig. 2.6 The two panels show the spatial differential conductance of an under-doped $\text{Bi}_2\text{Sr}_2\text{CaCu}_2\text{O}_{8+\delta}$ sample at $E = 50\text{meV}$ acquired in the same field of view. The *left panel* was acquired with a setpoint bias of $V_S = 150\text{mV}$ while the *right* with one of $V_S = 50\text{mV}$

the left was measured with $V_S = 150\text{mV}$ setup bias while the right with $V_S = 50\text{mV}$. It is clear that the spatial patterns of the same set of states in the material are imaged differently based on the setup bias parameter.

In order to faithfully resolve which modulations in $g(\vec{r}, E)$ arise from which energies in the LDOS, one must find a setup bias, V_S , for which $\int_0^{eV_S} n(\vec{r}, \epsilon) d\epsilon$ does not exhibit any modulations at the wave-vector of interest. In general, this is difficult because if $n(\vec{r}, E)$, for $E < eV_S$, has modulations at wave-vector \vec{Q} then it is likely that $\int_0^{eV_S} n(\vec{r}, \epsilon) d\epsilon$ also will, unless there is an evolution of the modulation phase with energy.

In cases where no suitable set-point can be found, we can use ratios of $g(\vec{r}, E = eV)$ at different voltages, typically of equal magnitude but opposite polarity. Such combinations have the effect of cancelling the setup effect described here and will be discussed in the following section.

2.4.2 Spectroscopic Functions $g(\vec{r}, E)$, $I(\vec{r}, E)$, $Z(\vec{r}, E)$, and $R(\vec{r}, E)$

I will now consider how, by defining new spectroscopic functions, one can remove the setup effect described in Sect. 2.4.1. Equations 2.35 and 2.36 show us that at a given location, \vec{r} , and setup bias, V_S , the conductance and current values at all bias voltages contain the same constant factor $I_S / \int_0^{eV_S} n(\epsilon, \vec{r}) d\epsilon$. Thus, by defining a

function that is a ratio of two conductances or currents at the same location, one obtains a function that is independent of V_S and hence setup effect free. In doing so, however, one must combine conductance or current values from different bias voltages and convolve LDOS modulations from different energies.

In this thesis the two setup free functions analysed are

$$Z(\vec{r}, |E|) = \frac{g(\vec{r}, +|E|)}{g(\vec{r}, -|E|)} = \frac{n(\vec{r}, +|E|)}{n(\vec{r}, -|E|)}, \quad (2.37)$$

and

$$R(\vec{r}, |E|) = \frac{I(\vec{r}, +|E|)}{I(\vec{r}, -|E|)} = \frac{\int_0^{|E|} n(\vec{r}, \epsilon) d\epsilon}{\int_0^{|E|} n(\vec{r}, -\epsilon) d\epsilon}. \quad (2.38)$$

These functions remove the setup effect by sacrificing the distinction between filled and empty states (negative and positive bias voltages respectively). $Z(\vec{r}, |E|)$ is the ratio of tunnelling probabilities for states at opposite polarity bias and similarly $R(\vec{r}, |E|)$ is the ratio of integrated tunnelling probabilities. As such they are often called tunnelling asymmetries.

One effect of these functions is that they naturally enhance any modulations present in the tunnelling conductance that have a π phase shift between states above and below the Fermi energy. As we will see in Chap. 4, this is the case for the predominantly d -symmetry form factor CDW present in $\text{Bi}_2\text{Sr}_2\text{CaCu}_2\text{O}_{8+\delta}$ and $\text{Na}_x\text{Ca}_{2-x}\text{CuO}_2\text{Cl}_2$. The use of $Z(\vec{r}, |E|)$ and $R(\vec{r}, |E|)$ naturally enhances the signals arising from these phenomena.

While $Z(\vec{r}, |E|)$ measures the tunnelling asymmetry between states at energies eV above and below the Fermi energy, $R(\vec{r}, |E|)$ measures the tunnelling asymmetry of all states up to an energy eV above and below the Fermi energy. $R(\vec{r}, |E|)$ then naturally gains a greater weight from modulations that are non-dispersive in energy, such as those from a charge density wave.

The final benefit of $Z(\vec{r}, |E|)$ and $R(\vec{r}, |E|)$ is that they correct for digitisation errors in the junction setup process. This is not a fundamental problem (as with the setup effect) but a purely technical malady. The high voltages applied to the piezo scanner tube are produced by a 16-bit digital to analogue converter (DAC) whose output is passed through a high voltage amplifier. The bin size of the DAC then determines a precision with which the set-point current can be attained by z -axis motion of the STM tip. This means that all pixels in an STM are taken at very slightly different values of I_S . Under the low mechanical and electrical noise conditions used for data acquisition in this thesis, this can be the dominant source of noise in the Fourier transform of $g(\vec{r}, V)$. Luckily, Eqs. 2.35–2.38 imply that this effect is cancelled exactly in $Z(\vec{r}, |E|)$ and $R(\vec{r}, |E|)$.

2.5 Experimental Apparatus

I will now describe briefly the specific experimental implementation of cryogenic SI-STM used to collect the data presented in this thesis.

2.5.1 STM Head

The STMs used in these studies all follow a construction similar to that shown in Fig. 2.7. Their design and construction is detailed in Ref. [17].

The STM tip is held atop a split electrode piezoelectric tube. By applying voltages to the electrodes, the x, y and z position of the tip can be controlled with sub-Angström precision over a total range of $\sim 1 \mu\text{m}$. This tube is held inside a sapphire prism. This can be actuated up and down by the slip-stick motion of shear piezo stacks, giving coarse positioning in the z-direction. This assembly is housed inside a rigid Macor body, designed to give its vibrational modes as high a frequency as possible.

Sample are inserted into the top of the STM head on brass sample holders which mate with the head assembly and are held tightly in place by a BeCu spring plate. This plate also applies the bias voltage to the sample, with the tip being held at ground.

Unless otherwise stated all measurements reported in this thesis were made using a chemically etched tungsten STM tip.

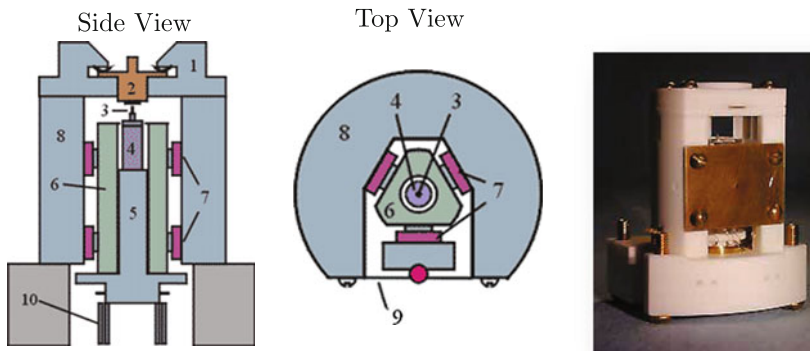


Fig. 2.7 Schematic drawing and photograph of STM head. Parts labelled 1–10 are: (1) Sample Receptacle (2) Sample Holder (3) Tip (4) Piezo-tube Scanner (5) Scanner Holder (6) Sapphire Prism (7) Shear Piezo Stacks (8) Macor Body (9) BeCu Spring Plate (10) Capacitive Position Sensor

2.5.2 Cryogenics

The data presented in this thesis were taken at temperatures between 45 K and 45 mK. All instruments were mounted in vacuum cans immersed in liquid ^4He resulting in a cryogenic ultra-high vacuum where the STM head is housed. The measurements presented in Chaps. 5 and 7 utilise a dilution refrigerator.

All samples were inserted from room temperature into the vacuum using an insertion rod and cleaved at ~ 4 K. From here they were then inserted directly into the STM head.

2.5.3 Vibration and RF Isolation

Mechanical vibrations introduce noise into STM measurements primarily by varying the tip-sample distance. To maximise the signal to noise ratio of our measurement we utilise passive vibration isolation. This method relies on successive stages having very different resonant frequencies. A concrete block (~ 10 tonnes, $f_{\text{res}} \sim 1$ Hz) is separated from the foundations of the building and supported on air springs. The cryostat is then suspended from a vibrational isolation table (~ 1 tonne, $f_{\text{res}} \sim 10$ Hz), again using air springs.

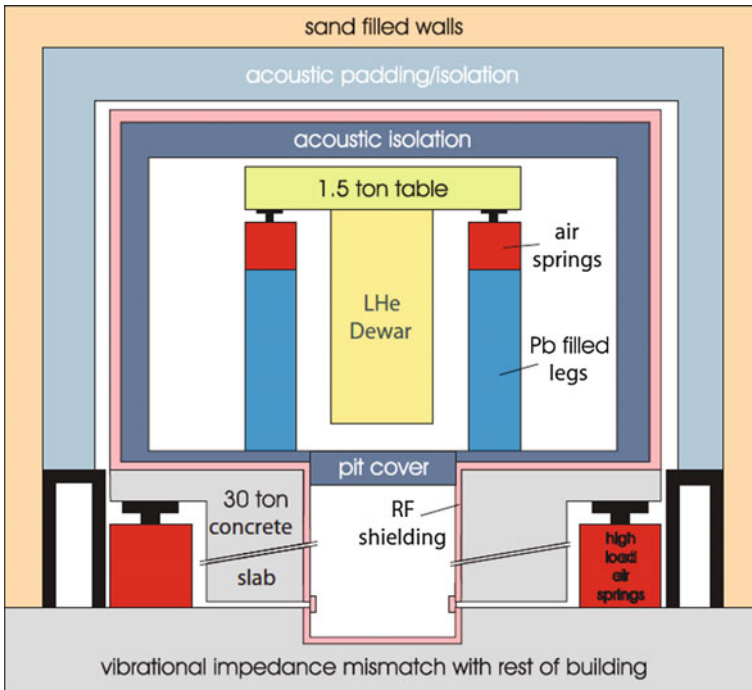


Fig. 2.8 Passive vibration isolation utilised in SI-STM experiments. Reproduced from Ref. [18]

Acoustic isolation is achieved by constructing a room around the cryostat on the floating block, incorporating sound absorbing material. This is then housed inside another room whose walls are filled with sand and the interior lined with sound absorbing material. This is shown in Fig. 2.8.

For the scanned Josephson experiments reported in Chaps. 5 and 7 the floating experimental room is RF shielded.

2.5.4 Instrumentation

The instrumentation used in our SI-STM measurements is shown in Fig. 2.9. Tip-sample current measurements are made with a low-noise current to voltage pre-

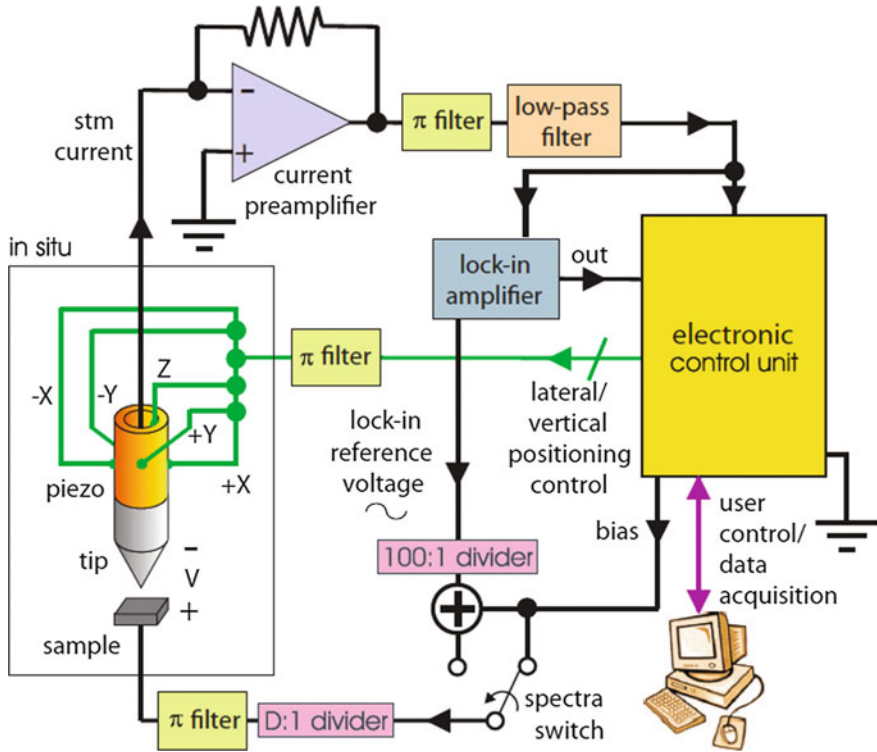


Fig. 2.9 A bias applied to the sample is sourced from the electronic control unit (ECU), a Topometrix SPM controller. The resulting tunnelling current is measured using a low noise current-voltage pre-amplifier situated at the cryostat head in the floating experimental room. The position of the tip is controlled by a piezoelectric scanner tube. The control voltages for this are supplied by the ECU. In topographic mode the z piezo-tube voltage is controlled by a PID feedback loop in the ECU to keep the tunnelling current constant. In spectroscopic mode, this feedback loop is turned off and a constant z piezo voltage used. An AC bias modulation from a lock-in amplifier is added to the sample bias. This lock-in amplifier measures the differential conductance through the resulting AC modulation in the tunnelling current. Reproduced from Ref. [20]

amplifier situated inside the floating experimental room. Differential conductance measurements are made using a lock-in amplifier. The DC bias voltage, feedback loop and high voltage signal to control the piezoelectrics are provided by a Topometrix SPM controller, interfaced to a computer running custom designed control software [19].

2.6 Cuprate Materials

In this thesis, SI-STM and SJTM are applied to cuprate superconductors to visualise charge density wave (CDW) modulations as well as those in the Cooper-pair condensate. Here I will briefly describe the cuprate samples studied.

The common feature of all cuprate superconductors are the CuO_2 planes. The variety in this family of materials arises from how these planes are incorporated into a crystal. In this thesis measurements of two cuprate materials, $\text{Bi}_2\text{Sr}_2\text{CaCu}_2\text{O}_{8+\delta}$ and $\text{Na}_x\text{Ca}_{2-x}\text{CuO}_2\text{Cl}_2$, are presented. These materials were chosen for their compatibility with SI-STM because they both cleave easily and reproducibly to yield atomically flat surfaces that are not reconstructed. Below I will briefly describe the crystallography and properties of these two cuprate superconductors, as well as the fabrication of the samples measured in our studies.

2.6.1 $\text{Bi}_2\text{Sr}_2\text{CaCu}_2\text{O}_{8+\delta}$

In $\text{Bi}_2\text{Sr}_2\text{CaCu}_2\text{O}_{8+\delta}$ the CuO_2 planes are sandwiched between BiO, SrO and Ca layers, as shown in Fig. 2.10. There are two CuO_2 layers per BiO layer, leading to the description of $\text{Bi}_2\text{Sr}_2\text{CaCu}_3\text{O}_{10+\delta}$ as a bi-layer compound, with $\text{Bi}_2\text{Sr}_2\text{CuO}_{6+\delta}$ and $\text{Bi}_2\text{Sr}_2\text{Ca}_2\text{Cu}_2\text{O}_{8+\delta}$ being its single and triple layer relatives respectively. $\text{Bi}_2\text{Sr}_2\text{CaCu}_2\text{O}_{8+\delta}$ has the I_4/mmm space group with 4 CuO_2 planes per unit cell, with an offset of $(1/2, 0, 0)$ between the two bilayers. The mirror plane between adjacent BiO layers leads to BiO being the natural cleave plane of the material. Note that bismuth atoms always lie directly above copper atoms, allowing one to determine the copper positions from the surface topography. The nearest neighbour distance between copper atoms forming approximately square lattice planes is 3.82\AA .

The CuO_2 plaquettes are not exactly square in $\text{Bi}_2\text{Sr}_2\text{CaCu}_2\text{O}_{8+\delta}$ due to the presence of a bulk incommensurate structural super-modulation [21, 22]. This buckling of the whole crystal, at 45° to the Cu-O directions (along the b-axis in Fig. 2.10) results from a lattice mismatch between the BiO and other layers of the crystal. Importantly, this modulation leaves intact a mirror symmetry between the two Cu-O directions in the CuO_2 plane. Thus, any breaking of this symmetry is spontaneous.

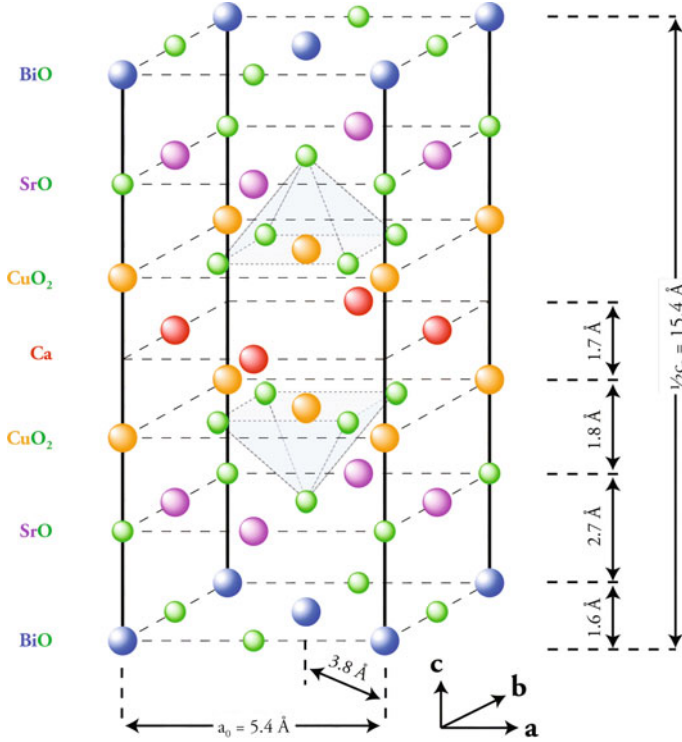
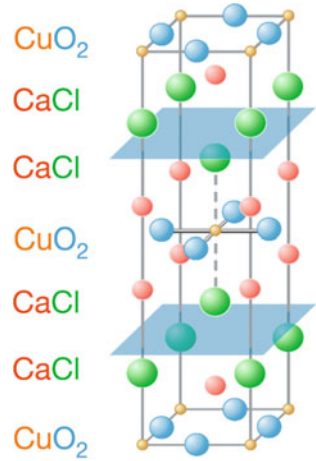


Fig. 2.10 Cartoon unit cell of the bi-layer cuprate $\text{Bi}_2\text{Sr}_2\text{CaCu}_2\text{O}_{8+\delta}$. CuO_2 planes are incorporated between Ca, SrO and BiO layers. Only half of the unit cell is shown along the c-axis. The second half of the unit cell is a repeat of that shown but offset by $(1/2, 0, 0)$. The natural cleavage plane is the BiO layer. Bi atoms are directly above the Cu atoms in the crystal structure allowing the Cu positions to be identified from surface topography. Reproduced from Ref. [23]

The $\text{Bi}_2\text{Sr}_2\text{CaCu}_2\text{O}_{8+\delta}$ samples used for the measurements presented here were grown by K. Fujita in the group of S. Uchida at the University of Tokyo. For hole dopings $p \leq 0.08$ $\text{Bi}_{2.2}\text{Sr}_{1.8}\text{Ca}_{0.8}\text{Dy}_{0.2}\text{Cu}_2\text{O}_{8+\delta}$ samples were used whereas for $p > 0.08$ the composition $\text{Bi}_{2.1}\text{Sr}_{1.9}\text{CaCu}_2\text{O}_{8+\delta}$ was employed.

High-quality single crystals were grown using the travelling solvent floating zone method. The samples were synthesised from dried powders of Bi_2O_3 , SrCO_3 , CaCO_3 and CuO . The crystal growth was carried out in air and at growth speeds of 0.15–0.2 mm/h for all samples. Annealing was used to vary the hole doping of each sample. Oxidation annealing is performed in air or under oxygen gas flow, and deoxidation annealing is done in vacuum or under nitrogen gas flow. Inductively coupled plasma spectroscopy was used for the composition analysis and a vibrating sample magnetometer was used for measurement of T_c . Each sample was inserted into the cryogenic ultra-high vacuum of the SI-STM system and cleaved at $T \approx 4\text{ K}$ to reveal an atomically flat BiO surface.

Fig. 2.11 Cartoon unit cell of $\text{Na}_x\text{Ca}_{2-x}\text{CuO}_2\text{Cl}_2$. CuO_2 planes are incorporated between CaCl layers. Hole doping is achieved by substituting Ca^{2+} ions for Na^+ ions, introducing holes into the CuO_2 planes. Reproduced from Ref. [25]



2.6.2 $\text{Na}_x\text{Ca}_{2-x}\text{CuO}_2\text{Cl}_2$

The other material for which measurements are reported in this thesis is $\text{Na}_x\text{Ca}_{2-x}\text{CuO}_2\text{Cl}_2$. In this material the CuO_2 planes are incorporated between CaCl layers, as shown in Fig. 2.11. The material is tetragonal, with the I_4/mmm space group and does not have any incommensurate structural super-modulation. Hole doping is achieved by substituting Ca^{2+} ions for Na^+ ions, introducing holes into the CuO_2 planes. In this thesis I present data from $\text{Na}_x\text{Ca}_{2-x}\text{CuO}_2\text{Cl}_2$ samples with $p = 12\%$.

The $\text{Na}_x\text{Ca}_{2-x}\text{CuO}_2\text{Cl}_2$ samples were grown by Y. Kohsaka at the University of Tokyo [24]. A flux method was used for growth, with high pressures used to increase the solubility of Na. The samples were synthesised from powders of $\text{Ca}_2\text{CuO}_2\text{Cl}_2$, NaClO_4 and NaCl in a high pressure anvil cell at pressures of 2–5.5 GPa.

2.7 Quasi-Particle Interference in Cuprates

Quasi-particle interference (QPI) is a technique used to extract the energy-momentum dispersion of quasi-particles in a material using SI-STM [2, 3, 26]. It uses the characteristic wave-lengths present in the density of states modulations formed by quasi-particles scattering from impurities, often called Friedel oscillations. With a suitable model, one can use the bias voltage dependence of these characteristic wave-lengths to determine the quasi-particle dispersion.

This technique is applicable to both normal Landau quasi-particles as well as Bogoliubov quasi-particles in a superconductor. In Chap. 4 I will use Bogoliubov quasi-particle interference in $\text{Bi}_2\text{Sr}_2\text{CaCu}_2\text{O}_{8+\delta}$ to determine geometric details of the Fermi surface. In the following I will outline how this technique works and its specific application to cuprates.

2.7.1 QPI - A Qualitative Understanding

For a clean metal where the quasi-particle states are described by Bloch functions, $\Psi_{\vec{k}} = e^{i\vec{k}\cdot\vec{r}}u_{\vec{k}}(\vec{r})$, the spatial dependence of the LDOS, $n(\vec{r}, E = eVs) = \sum_{\vec{k}} |\Psi_{\vec{k}}|^2 \delta(E - \epsilon_{\vec{k}})$, only contains modulations with the periodicity of the atomic lattice, encoded in $u_{\vec{k}}$.

The introduction of impurities into the lattice leads to elastic scattering between Bloch states, which are no longer the true eigenstates. The new eigenstates will be linear superpositions of Bloch states that lie on the same constant energy contour in \vec{k} -space. This mixing of \vec{k} -states leads to oscillations in $n(\vec{r}, E)$ with wave-vectors $\{\vec{q}\}$ linking points on the contour of constant energy E . This can be illustrated as follows:

$$|\Psi(\vec{r})|^2 = |a_1 u_{\vec{k}_1}(\vec{r}) e^{i\vec{k}_1 \cdot \vec{r}} + a_2 u_{\vec{k}_2}(\vec{r}) e^{i\vec{k}_2 \cdot \vec{r}}|^2 \quad (2.39)$$

$$= |a_1 u_{\vec{k}_1}(\vec{r})|^2 + |a_2 u_{\vec{k}_2}(\vec{r})|^2 + (a_1 u_{\vec{k}_1}(\vec{r}) a_2^* u_{\vec{k}_2}^*(\vec{r}) e^{i\vec{q} \cdot \vec{r}} + c.c) \quad (2.40)$$

where $\vec{q} = \vec{k}_1 - \vec{k}_2$. This will be observed as modulations of the local density of states, $n(\vec{r}, E)$ with wavelength $\lambda = \frac{2\pi}{|\vec{q}|}$.

As discussed above in Sect. 2.4, SI-STM yields spectroscopic maps $I(\vec{r}, E)$ and $g(\vec{r}, E)$. Further, $g(\vec{r}, E)$ is proportional to the local density of states $n(\vec{r}, E)$. For a fixed energy, $g(\vec{r}, E)$ is a two-dimensional image and will contain quasi-particle interference modulations from scattering between the contours of constant energy E . By taking a two-dimensional Fourier transform to yield $\tilde{g}(\vec{q}, E)$ we can extract the LDOS modulation wave-vectors and hence infer geometric information about the constant energy contours (CCEs) in the quasi-particle dispersion. By tracking the wave-vectors present in these Fourier transforms systematically with energy we can potentially extract the quasi-particle dispersion in a material.

To illustrate this consider a quasi-2D material with a cylindrical Fermi surface with Fermi wavevector $|\vec{k}_F|$ in the presence of a point impurity (whose scattering form factor will be momentum independent). The power spectrum of a conductance map taken at zero bias will show a strong cusp at a circle of radius $|\vec{q}| = 2|\vec{k}_F|$ because this is where the joint density of states for scattering is largest.

In this example it is easy to work backwards from the power spectrum to deduce the Fermi-surface and by varying the bias we can determine the dispersion relation. However, in cases where the scattering potential is not isotropic or the constant energy contours are complicated this process becomes non-trivial and is one of the major challenges of analysing this type of experiment. Luckily in cuprates, we have a well established model of Bogoliubov quasi-particle interference called the ‘‘octet model’’, which I will now introduce.

2.7.2 The Octet Model

It is well established that cuprate superconductors exhibit a d -wave superconducting gap of the form,

$$\Delta_{\vec{k}} = \frac{\Delta_0}{2} (\cos(k_x a_0) - \cos(k_y a_0)) , \quad (2.41)$$

with four nodes along the zone diagonals. This leads to a Bogoliubov quasi-particle dispersion

$$E_{\vec{k}} = \sqrt{\epsilon_{\vec{k}}^2 + \Delta_{\vec{k}}^2} , \quad (2.42)$$

where $\epsilon_{\vec{k}}$ is the dispersion of the underlying normal band. In the cuprates $\partial_{k_{\perp}} \Delta_{\vec{k}} \ll \partial_{k_{\parallel}} \epsilon_{\vec{k}}$ ($\partial_{k_{\parallel}} \epsilon_{\vec{k}} / \partial_{k_{\perp}} \Delta_{\vec{k}} \approx 20$ at the gap nodes [27]), where k_{\perp} and k_{\parallel} are perpendicular and parallel to the Fermi wave-vector respectively. This results in banana-like constant energy contours (CECs) in the Bogoliubon dispersion as shown in the Fig. 2.12.

As discussed in the previous section, the strongest modulations are usually seen at wave-vectors for which the joint density of states for scattering between points on the CECs are maximal. One way this can arise is through nesting, where large sections of a Fermi surface are parallel to each other in \vec{k} -space.

In cuprates the situation is different. The points with the largest density of states

$$n(\vec{k}, E) \propto \frac{1}{|\nabla_{\vec{k}}(E)|} \quad (2.43)$$

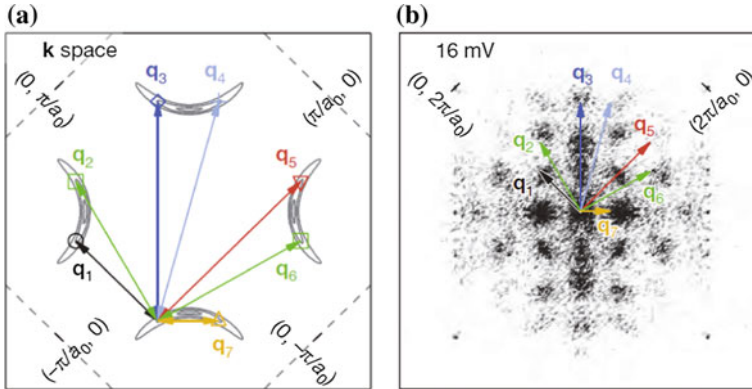


Fig. 2.12 **a** Banana shaped constant energy contours (CECs) of the d -wave Bogoliubov quasi-particle dispersion in \vec{k} -space. In the octet model, quasi-particle interference modulations in the LDOS primarily arise from scattering between the eight tips of these bananas. This results in 7 scattering vectors $\vec{q}_1, \dots, \vec{q}_7$. **b** Measured fourier transform $Z(\vec{q}, |E|)$ from underdoped $\text{Bi}_2\text{Sr}_2\text{CaCu}_2\text{O}_{8+\delta}$ shown LDOS modulations at the wave-vectors $\vec{q}_1, \dots, \vec{q}_7$. Reproduced from Ref. [2]

are those at the eight tips of the banana like CECs. In the absence of nesting, the largest joint density of states for scattering will also be between these eight points [8, 27]. Thus QPI LDOS modulations will arise from the set of $8 \times 7 = 56$ pairings that connect these.

These 56 pairings are not all distinct because the same scattering vector connects multiple points. Taking this into account there are 16 independent \vec{q} vector measurements that we can make at each bias voltage. But again, some of these are related by the crystal symmetry, allowing us to make multiple independent measurements of the 7 scattering vectors,

$$\vec{q}_1(E) = (2k_x, 0) \quad (2.44)$$

$$\vec{q}_2(E) = (k_x + k_y, k_y - k_x) \quad (2.45)$$

$$\vec{q}_3(E) = (k_x + k_y, k_x + k_y) \quad (2.46)$$

$$\vec{q}_4(E) = (2k_x, 2k_y) \quad (2.47)$$

$$\vec{q}_5(E) = (0, 2k_y) \quad (2.48)$$

$$\vec{q}_6(E) = (k_x - k_y, k_x + k_y) \quad (2.49)$$

$$\vec{q}_7(E) = (k_x - k_y, k_y - k_x), \quad (2.50)$$

where $\vec{k} = (k_x, k_y)$ corresponds to the momentum space coordinates of the banana tips at a given energy.

Ultimately, we wish to determine an energy momentum-dispersion relation $\vec{k}(E)$. To do this we can invert Eqs. 2.44–2.50 to yield,

$$2k_x(E) = |\vec{q}_1|, q_{2x} - q_{2y}, q_{6y} - q_{6x}, |\vec{q}_3 - \vec{q}_7|/\sqrt{2}, |\vec{q}_5| - \sqrt{2}|\vec{q}_7|, q_{4x} \quad (2.51)$$

$$2k_y(E) = |\vec{q}_5|, q_{2x} + q_{2y}, q_{6y} + q_{6x}, |\vec{q}_3 + \vec{q}_7|/\sqrt{2}, \sqrt{2}|\vec{q}_7| - |\vec{q}_1|, q_{4y}. \quad (2.52)$$

These expressions show that this octet model is geometrically over-constrained. At each energy, E , we are able to make 6 independent estimates of $\vec{k}(E)$. Although I have given some justification for this octet model above, its strength lies in its geometrical over-determination. That the 6 independent estimates of $\vec{k}(E)$ agree demonstrates that the octet model is an internally consistent model of QPI in cuprates.

Having measured $\vec{k}(E)$, how should we interpret this information? Due to the condition $\partial_{\vec{k}} \Delta_{\vec{k}} \ll \partial_{\vec{k}} \epsilon_{\vec{k}}$ being realised in cuprates, and Eq. 2.41, $E \approx \Delta_{\vec{k}}$. For every measurement energy, the superconducting gap takes this value at the position $\vec{k}(E)$ in momentum space. Thus we can directly determine the momentum space gap function as shown in Fig. 2.13.

As can be seen in Fig. 2.12, the tips of the banana shaped CECs lie very close to the position of the underlying Fermi surface in momentum space. Thus, by plotting all of the points $\vec{k}(E)$, one can trace out the position of the Fermi surface in momentum space as shown in Fig. 2.13.

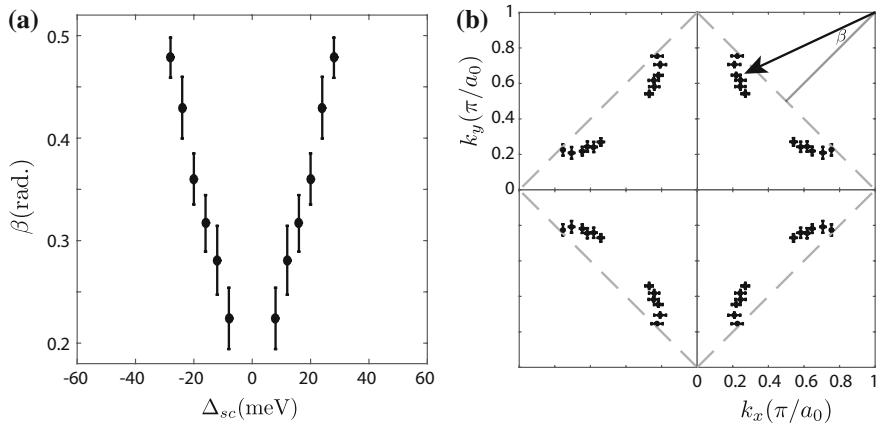


Fig. 2.13 **a** d -wave superconducting gap function measured for $\text{Bi}_2\text{Sr}_2\text{CaCu}_2\text{O}_{8+\delta}$ with $p = 17\%$ using quasi-particle interference. Gap values are plotted against β , the angle from the nodal (π, π) directions. **(b)** (k_x, k_y) values of all points shown in **a**. They trace out the underlying Fermi surface. In $\text{Bi}_2\text{Sr}_2\text{CaCu}_2\text{O}_{8+\delta}$ with $p < 19\%$ no quasi-particle interference is observed from quasi-particles beyond the anti-ferromagnetic Brillouin zone (*dashed lines*). Plotted points represent the mean of 6 independent k_x and k_y estimates made from measured wave-vectors $\vec{q}_1, \dots, \vec{q}_7$ using Eqs. 2.51 and 2.52. Error bars represent the standard deviation of these 6 independent estimates

This technique will be used in Chap. 4 to extract the Fermi surface geometry of $\text{Bi}_2\text{Sr}_2\text{CaCu}_2\text{O}_{8+\delta}$ for a range of dopings. Here, instead of using the full octet of scattering vectors, \vec{q}_4 alone is used. The set of relations Eqs. 2.51 and 2.52 show that this is sufficient.

2.8 Mapping Spatial Variations in the Amplitude and Phase of LDOS Modulations

SI-STM spectroscopic maps contain a vast amount of information, with modulations occurring on multiple length scales and in multiple directions. Often we are only interested in the amplitude and phase of a small sub-set of these modulations. These quantities can be extracted from our data sets by filtering their complex Fourier transforms so that only wave-vectors proximal to those of interest remain. For instance, if we are interested in modulations of the spectroscopic map $M(\vec{r}, E)$ at wave-vector \vec{Q} we would filter its Fourier transform $\tilde{M}(\vec{q}, E)$ to yield

$$M_{\vec{Q}}(\vec{q}, E) = \tilde{M}(\vec{q}, E) e^{-\frac{(\vec{q}-\vec{Q})^2}{2\Lambda^2}}, \quad (2.53)$$

where Λ^{-1} is the characteristic length scale below which variations in the amplitude or phase of modulations at \vec{Q} will not be resolved in this process. I will refer to this process as Fourier filtration.

Using an inverse Fourier transform one can then proceed to create the complex real-space map,

$$M_{\vec{Q}}(\vec{r}, E) = \frac{2}{(2\pi)^2} \int d\vec{q} e^{i\vec{q} \cdot \vec{r}} \tilde{M}_{\vec{Q}}(\vec{q}, E), \quad (2.54)$$

that only contains modulations at wave-vectors proximal to \vec{Q} .

To make a real-space map of modulations at wave-vector \vec{Q} one simply takes the amplitude of $M_{\vec{Q}}(\vec{r})$,

$$A_{\vec{Q}}(\vec{r}, E) = \sqrt{(Re M_{\vec{Q}}(\vec{r}, E))^2 + (Im M_{\vec{Q}}(\vec{r}, E))^2}. \quad (2.55)$$

Similarly the phase of these modulations, $\phi(\vec{r})$, is given by

$$\phi(\vec{r}) = \arctan \frac{Im M_{\vec{Q}}(\vec{r}, E)}{Re M_{\vec{Q}}(\vec{r}, E)}. \quad (2.56)$$

In other cases we are interested in removing a specific Fourier component from an image because it is visually dominating and we wish to examine a smaller modulation at another wave-vector. In this case we can remove those modulations at wave-vectors $\pm \vec{Q}'$ to create the real-space map

$$M'_{\pm \vec{Q}}(\vec{r}, E) = \frac{2}{(2\pi)^2} \int d\vec{q} e^{i\vec{q} \cdot \vec{r}} \left[\tilde{M}(\vec{q}, E) - \tilde{M}'_{\pm \vec{Q}}(\vec{q}, E) \right], \quad (2.57)$$

where

$$M'_{\pm \vec{Q}}(\vec{q}, E) = \tilde{M}(\vec{q}, E) \times \left[e^{-\frac{(\vec{q} - \vec{Q}')^2}{2\Lambda^2}} + e^{-\frac{(\vec{q} + \vec{Q}')^2}{2\Lambda^2}} \right]. \quad (2.58)$$

References

1. G. Binnig, H. Rohrer, Scanning tunneling microscopy. *Surf. Sci.* **126**(126), 236–244 (1982)
2. K. Fujita et al., Spectroscopic imaging scanning tunneling microscopy studies of electronic structure in the superconducting and pseudogap phases of cuprate high-*t_c* superconductors. *J. Phys. Soc. Jpn.* **81**(1), 011005 (2012)
3. A. Yazdani, E.H. da Silva Neto, P. Aynajian, Spectroscopic imaging of strongly correlated electronic states. *Ann. Rev. Condensed Matter Phys.* **7**(1), 11–33 (2016)
4. L. Esaki, New phenomenon in narrow germanium p-n junctions. *Phys. Rev.* **109**(2), 603–604 (1958)
5. I. Giaever, Energy gap in superconductors measured by electron tunneling. *Phys. Rev. Lett.* **5**(4), 147–148 (1960)
6. J. Bardeen, Tunnelling from a many-particle point of view. *Phys. Rev. Lett.* **6**(2), 6–8 (1961)
7. M.H. Cohen, L.M. Falicov, J.C. Phillips, Superconductive tunneling. *Phys. Rev. Lett.* **8**(8), 316–318 (1962)
8. J. Hoffman, Search for alternative electronic order in the by scanning tunneling high temperature superconductor $\text{Bi}_2\text{Sr}_2\text{CaCu}_2\text{O}_{8+\delta}$ by scanning tunneling microscopy. Ph.D. thesis. University of California, Berkeley (2003)

9. W.A. Harrison, Tunneling from an independent-particle point of view. *Phys. Rev.* **123**(1), 85–89 (1961)
10. J. Bardeen, L.N. Cooper, J.R. Schrieffer, Theory of superconductivity. *Phys. Rev.* **108**(5), 1175–1204 (1957)
11. B. Josephson, Possible new effects in superconductive tunnelling. *Phys. Lett.* **1**(7), 251–253 (1962)
12. J. Bardeen, Tunneling into superconductors. *Phys. Rev. Lett.* **9**(4), 147–149 (1962)
13. M. Tinkham, *Introduction to Superconductivity* (McGraw-Hill Book Co., New York, 1975)
14. *Adapted from IAP/TU Wien STM Gallery under Creative Commons Attribution ShareAlike 2.0 Austria License*
15. J. Tersoff, D.R. Hamann, Theory of the scanning tunneling microscope. *Phys. Rev. B* **31**(2), 805–813 (1985)
16. C.J. Chen, *Introduction to Scanning Tunneling Microscopy* (Oxford University Press, Oxford, 2007), pp. 1–40
17. S.H. Pan, E.W. Hudson, J.C. Davis, ³He refrigerator based very low temperature scanning tunneling microscope. *Rev. Sci. Instrum.* **70**(2), 1459 (1999)
18. M.H. Hamidian, Imaging the Realm of the Strongly Correlated: Visualising Heavy Fermion Formation and The Impact of Kondo Holes in URu₂Si₂. Ph.D. thesis. Cornell University (2011)
19. E.W. Hudson, Investigating High-T_c Superconductivity on the Atomic Scale by Scanning Tunneling Microscopy (1994)
20. C.B. Taylor, Coexistence of Bogoliubov Quasiparticles and Electronic Cluster Domains in Lightly Hole-Doped Cuprate Superconductors. Ph.D. thesis. Cornell University (2008), p. 211
21. M. Zhiqiang et al., Relation of the superstructure modulation and extra-oxygen local-structural distortion in Bi. *Phys. Rev. B* **55**(14), 9130–9135 (1997)
22. X.B. Kan, S.C. Moss, Fourdimensional crystallographic analysis of the incommensurate modulation in a Bi₂Sr₂CaCu₂O₈ single crystal. *Acta Crystallogr. Sect. B* **48**(2), 122–134 (1992)
23. J.A. Slezak, Atomic-Scale Impact of Unit Cell Dimensions on Pairing in a High-Temperature Superconductor. Ph.D. thesis. Cornell University (2007)
24. Y. Kohsaka et al., Growth of Na-doped Ca₂CuO₂Cl₂ single crystals under high pressures of several GPa. *J. Am. Chem. Soc.* **124**(41), 12275–12278 (2002)
25. T. Hanaguri et al. A ‘checkerboard’ electronic crystal state in lightly hole-doped Ca_{2-x}NaxCuO₂Cl₂. *Nature* **430**, 1001–1005 (2004)
26. M.F. Crommie, C.P. Lutz, D.M. Eigler, Imaging standing waves in a two-dimensional electron gas. *Nature* **363**, 524 (1993)
27. Q.-H. Wang, D.-H. Lee, Quasiparticle scattering interference in high-temperature superconductors. *Phys. Rev. B* **67**(2), 020511 (2003)

Visualising the Charge and Cooper-Pair Density Waves
in Cuprates

Edkins, S.

2017, XVI, 187 p. 78 illus., 58 illus. in color., Hardcover

ISBN: 978-3-319-65974-9